Hindawi Publishing Corporation
EURASIP Journal on Image and Video Processing
Volume 2010, Article ID 871409, 10 pages
doi:10.1155/2010/871409

Research Article

Acquiring Multiview C-Arm Images to Assist Cardiac Ablation Procedures

Pascal Fallavollita

School of Computing, Queen's University, Kingston, ON, Canada K7L 3N6

Correspondence should be addressed to Pascal Fallavollita, pascal@cs.queensu.ca

Received 31 July 2009; Accepted 14 December 2009

Academic Editor: Jiebo Luo

CARTO XP is an electroanatomical cardiac mapping system that provides 3D color-coded maps of the electrical activity of the heart; however it is expensive and it can only use a single costly magnetic catheter for each patient intervention. Our approach consists of integrating fluoroscopic and electrical data from the RF catheters into the same image so as to better guide RF ablation, shorten the duration of this procedure, increase its efficacy, and decrease hospital cost when compared to *CARTO XP*. We propose a method that relies on multi-view C-arm fluoroscopy image acquisition for (1) the 3D reconstruction of the anatomical structure of interest, (2) the robust temporal tracking of the tip-electrode of a mapping catheter between the diastolic and systolic phases and (3) the 2D/3D registration of color coded isochronal maps directly on the 2D fluoroscopy image that would help the clinician guide the ablation procedure much more effectively. The method has been tested on canine experimental data.

1. Introduction

The current incidence of sudden cardiac death (SCD) in the United States is between 200 000 and 250 000 cases per year, with a worldwide incidence of 4 to 5 million cases per year [1]. The most common electrophysiological mechanism leading to SCD is tachyarrhythmia such as ventricular tachycardia (VT). Severe disorders of the heart rhythm that can lead to SCD are often treated by radio-frequency (RF) catheter ablation, which consists of inserting a catheter inside the heart, near the area from which originates the abnormal cardiac electrical activity, and delivering RF currents through the catheter tip so as to ablate the arrhythmogenic area (see Figure 1(a)). The precise localization of the arrhythmogenic site and positioning of the RF catheter at that site are problematic; they can impair the efficacy of the procedure and the procedure can last several hours, especially for complex arrhythmias. To shorten the duration of RF catheter ablation and increase its efficiency during the arrhythmia, four main commercial mapping systems that provide a 3D volume and color display of the cardiac chamber and electrical activation sequence have been developed. These include: *CARTO XP* (Biosense-Webster, Diamond Bar, CA, USA), *NavX* system (St Jude Medical, St Paul, MN, USA), *RPM* (Boston Scientific, Natick, MA, USA), and *LocaLisa* (Medtronic, Minneapolis, MN, USA). All these systems including purchase of system-specific catheters are costly for the modern day hospital.

Other approaches proposed by researchers to guide RF ablation therapy employ multimodal image fusion. These include the visualization of an optically tracked catheter by making use of magnetic resonance imaging (MRI) [2, 3], the combination of MRI and fluoroscopy [4], ultrasound imaging of the ablation catheter [5], the combination of ultrasound and preoperative computer tomography (CT) [6], or preoperative imaging (CT/MRI) for ablation planning [7, 8]. However, all these approaches omit incorporating electrophysiological data that is crucial for the clinician when locating the arrhythmogenic site.

Recently, efforts have been made in attempting to develop a more affordable fluoroscopic navigation system by obtaining local electrical activation times from a roving ablation catheter whose positions are computed from a single image using a monoplane C-arm fluoroscope. However, this single image method yielded inaccurate 3D reconstructions as depth estimations were about 10 mm, thus motivating the need of using multiview geometry for accurate 3D reconstruction. Research objectives were aimed at emulating

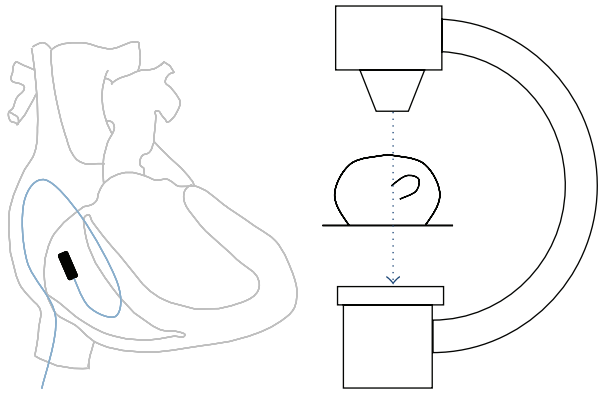

(a) (b)

Figure 1: (a) Ablation catheter and RF currents during energy delivery. (b) Monoplane C-arm fluoroscopic X-ray system to guide RF catheter ablation.

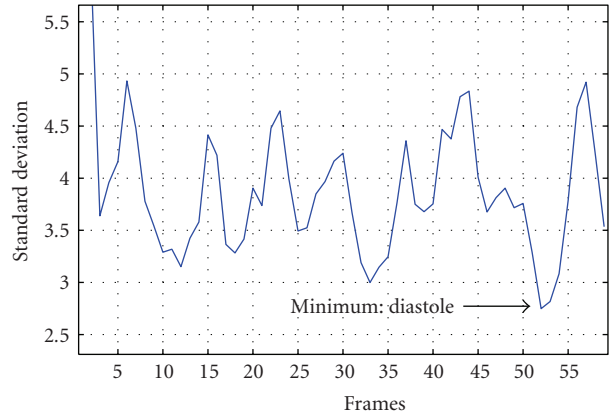

Figure 2: Standard deviation of the differences between successive frames during a one-second sequence (60 frames). Shown here is a sample curve depicting the image extraction algorithm and the diastole image frame number.

the format of the *CARTO XP* system and focusing on treating ventricular tachycardias [9]. With the *CARTO XP* nonfluoroscopic mapping approach, the patient is positioned over a tripod emitting three electromagnetic waves at unique frequencies. Each beam is registered by one of three specifically tuned coils embedded in the mapping catheter tip to specify location in 3D space, when the catheter tip is considered against a reference catheter. The catheter location and electrograms are recorded and reconstructed in realtime and presented as a 3D geometrical map color coded with the electrophysiological information. The arrhythmia must remain the same during the long point-by-point mapping procedure.

The emphasis of this paper is a continuation of the work in [9], but with a focus on multiview vision techniques. The long-term objective continues to develop a system similar to the functionality of the *CARTO XP* technology; albeit with the following advantages: (a) being more affordable by making use of cost-effective catheters which increase the number of available types and shapes of catheters used during the cardiac ablation procedure, (b) use of common monoplane C-arm X-ray fluoroscopes (see Figure 1(b)) compared to expensive new mapping equipment (>300,000$/system, >5,000$/catheter) that need to be purchased by hospitals, and (c) that 2D/3D registration using only X-ray fluoroscopy is possible in order to superimpose a translucent image of the cardiac activation map directly over 2D C-arm images.

The contributions of this paper are as follows: (i) we provide a complete analysis on two-view 3D reconstruction of the tip-electrode of a mapping catheter inserted in the left ventricle of the heart, (ii) we propose an automatic algorithm that extracts the fluoroscopy image depicting the diastolic image phase, (iii) we automatically filter and track the tip-electrode in a sequence of images using a 2D/2D registration algorithm initialized by clicking once on the tip electrode seen in the diastolic image, and (iv) we provide a detailed report on the feasibility of using our multiview 3D methodology to guide VT catheter ablation by presenting an experimental procedure and results on canine data.

2. Methodology

The overall workflow is summarized as follows. Once C-arm data acquisition is achieved, extracting relevant images is necessary in order to minimize motion artifacts before reconstruction in three dimensions. Thus, an image extraction algorithm is first presented allowing us to select images depicting important phases of the cardiac cycle. Second, we describe a single-click algorithm coupled with a new image processing scheme allowing for automatic temporal tracking of the tip electrode. We conclude the section by recalling the mathematics of multiview geometry and propose a fitting technique for 3D reconstruction purposes.

2.1. Fluoroscopic Image Analysis. As an alternative to electrocardiogram gating and to minimize motion blur in the C-arm images acquired, we developed the following algorithm to select the frame for each mapping site. The number of frames making up each sequence varied depending on how long the technician stepped on the C-arm foot pedal. In general, each sequence contained up to 200 frames. By calculating the standard deviation of the differences between all the pixels of two successive frames, we were able to visually determine that the frame showing the smallest standard deviation also had the least motion blur (see Figure 2). This frame represented the diastolic phase of the cardiac cycle. The maximum standard deviation occurred during the systolic phase.

2.2. Automatic Tracking of Tip-Electrode Using Single-Click Initialization. Locating the tip-electrode of the mapping catheter is crucial since it will come into contact with the arrhythmogenic site for ablation purposes. Therefore, extracting 2D coordinates of the tip electrode is essential. However, this is not an easy task when attempting to develop an automatic algorithm. To our knowledge, the work in [10] presents the most recent work focusing on this task. The authors present a steerable tensor voting filter to extract

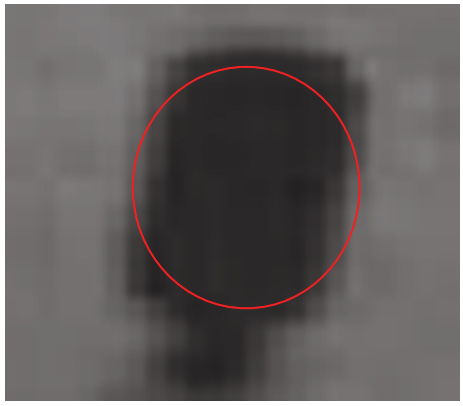

Figure 3: The tip-electrode of an ablation catheter approximated as a disk (circle).

the tip-electrode of ablation catheters and report results of approximately 70% accuracy for electrode detection in extremely noisy images. Nevertheless, the algorithm requires defining 3 tensor voting field parameters that require adjustment. The results are not clinically viable and manual selection is still necessary to collect all the tip-electrode coordinates in the C-arm images. At this stage, we thought it best to preserve a smooth workflow by manually selecting only the tip electrode visible in each of the diastole images.

2.2.1. Three-Step Filter to Catalyze Temporal Tracking. At each user-click of the tip-electrode, automatic tracking commences between the diastolic and systolic image frames determined in Section 2.1. Two cropped window sizes are first defined: (i) a 50×50 *template* window surrounding the tip electrode center, and a 100×100 *search window* around the *template*. For both cropped windows, we apply the following 3-step preprocessing filter.

A homomorphic filter is used first to denoise the fluoroscopic image [11]. The homomorphic filter decreases the contribution made by the low frequencies and amplifies the contribution of high frequencies. The result is simultaneous dynamic range compression and contrast enhancement. The homomorphic filter is given by

$$H(u,v) = (\gamma_H - \gamma_L)\left(1 - e^{-c(D^2(u,v)/D_o^2}\right) + \gamma_L \quad (1)$$

with $\gamma_L < 1$ and $\gamma_H > 1$. The coefficient c controls the sharpness of the slope at the transition between high and low frequencies; whereas D_o is a constant that controls the shape of the filter and $D(u,v)$ is the distance in pixels from the origin of the filter.

Anisotropic systems are those that exhibit a preferential spreading direction while isotropic systems are those that have no preferences. The Perona-Malik anisotropic diffusion [12] method was implemented here in order to reduce noise and texture from the image, as well as to preserve and enhance structures. The diffusion equation is given by

$$\frac{\partial I}{\partial t} = \operatorname{div}(c(x,y,t)\nabla I), \quad (2)$$

where I is the input image and $c(x,y,t)$ is the diffusion coefficient that controls the degree of smoothing at each image pixel. The diffusion coefficient is a monotonically decreasing function of the image gradient magnitude. It allows for locally adaptive diffusion strengths; edges are selectively smoothed or enhanced based on the evaluation of the diffusion function. Although any monotonically decreasing continuous function of the gradient would suffice as a diffusion function, we use the following diffusion coefficient:

$$c(x,y,t) = e^{-((|\nabla I|/K)^2)}. \quad (3)$$

K is referred to as the *diffusion constant* or the *flow constant*. The greatest flow is produced when the image gradient magnitude is close to the value of K. Therefore, by choosing K to correspond to gradient magnitudes produced by noise, the diffusion process can thus be used to reduce noise in images.

Morphological filtering was applied as a final image processing step in order to eliminate background elements around the primary coronary arteries. The structuring element consists of a pattern specified as the coordinates of a number of discrete points relative to a defined origin. Normally, Cartesian coordinates are a convenient way of representing an element as a small image on a rectangular grid. We chose a disk structuring element having a radius of a few pixels, since the contours of the tip-electrode of the mapping catheter can be modeled as a disk (see Figure 3). The structuring element will suppress the background (black) and enhance the arteries (grayscale). When a morphological operation is carried out, the origin of the structuring element is typically translated to each pixel position in the image in turn, and then the points within the translated structuring element are compared with the underlying image pixel values.

2.2.2. Temporal Tracking via 2D/2D Registration. Our method builds on the following intuition. As we are dealing with the same imaging modality during registration, then the electrode tip carries enough distinctive information for intensity-based registration to *hone in* the correct transformation (i.e., displacement) between image frames. Also, since the electrode structure is solid then a rigid-based 2D/2D registration scheme should suffice.

We implemented the Normalized Correlation (NC) metric. Pixel values are taken from the *search window*; their positions are mapped to the *template* image in order to find a match, or superposition of the two. The correlation is normalized by the autocorrelations of both the images [13]. Let *Img1* and *Img2* be the *search window* and *template* image, respectively. NC computes pixel-wise cross-correlation and normalizes it by the square root of the autocorrelation of the images:

$$NC = -1 \times \frac{\sum_{i=1}^{N}\left(\mathrm{Img1}_i \cdot \mathrm{Img2}_i\right)}{\sqrt{\sum_{i=1}^{N}\mathrm{Img1}_i^2 \cdot \sum_{i=1}^{N}\mathrm{Img2}_i^2}}, \quad (4)$$

where $\mathrm{Img1}_i$ and $\mathrm{Img2}_i$ are the ith pixels in two images, respectively, and N is the number of pixels considered. The

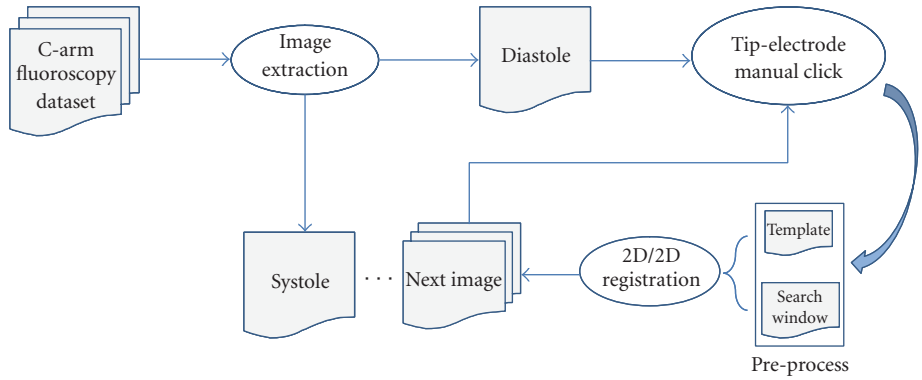

Figure 4: Workflow to acquire tip electrode coordinates in successive 2D images between the diastolic and systolic phase. A single click initialization launches a robust tracking routine.

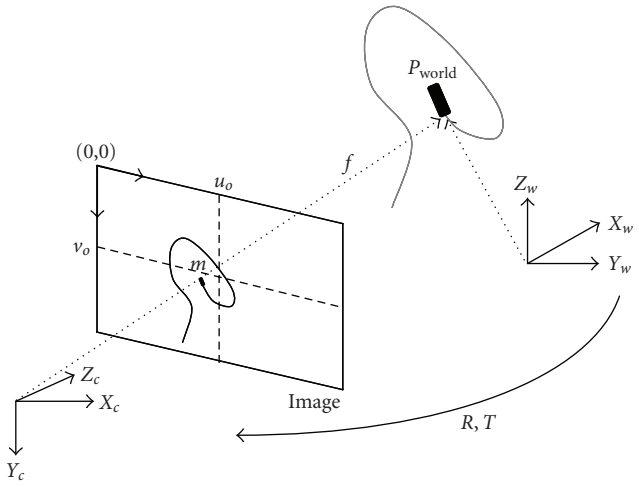

Figure 5: The perspective camera model. Any 3D world point can be projected onto a 2D plane and its coordinates would be (u, v) pixels.

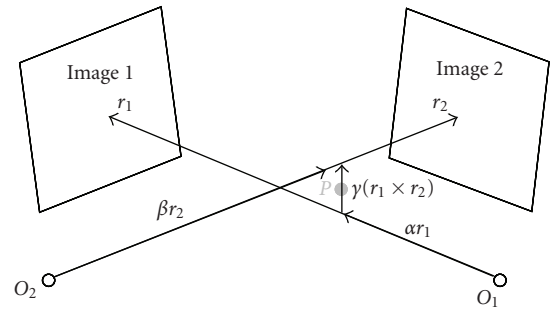

Figure 6: Stereo triangulation setup for the 3D reconstruction of corresponding points located in biplane images. Since both backprojected rays from camera O_1 and camera O_2 do not intersect, a solution is found by estimating a 3D point, P, which is half way between the two rays.

-1 factor is used to optimize the metric when its minimum is reached, say at minus one. Misalignment between the images results in small measurement values. This metric produces a cost function with sharp peaks and well-defined minima. The number of spatial samples used here is empirically set at 50.

The transform being updated is a simple Euler 2D transform which is composed of a plane rotation and a two-dimensional translation. The rotation is applied first, followed by the translation. Optimization was performed using the Levenberg-Marquardt algorithm and maximum iterations were set to a maximum of 100. Seeing how both images are relatively small to begin with, convergence should be relatively instant.

The next position of the tip electrode is obtained by calculating optimal transformation that locks both images over each other. The centroid is extracted and serves as 2D coordinates for the tip electrode in the image following the diastolic frame. Here, template and search window images are extracted again and registration is executed. This routine is performed until the systolic image (see Figure 4). At this stage we should have the estimated 2D coordinates of the tip electrodes in all images between diastole and systole.

2.3. C-Arm Fluoroscopy Geometry. If we define a three-dimensional point $P_{\text{world}} = [X\ Y\ Z\ 1]^T$ in the world coordinate system (see Figure 5), then its 2D projection in an image, $m = [u\ v\ 1]^T$, is achieved by constructing a projection matrix:

$$P_{FP} = \begin{bmatrix} kf & 0 & u_o \\ 0 & kf & v_o \\ 0 & 0 & 1 \end{bmatrix} \times \begin{bmatrix} r_{11} & r_{12} & r_{13} & t_x \\ r_{21} & r_{22} & r_{23} & t_y \\ r_{31} & r_{32} & r_{33} & t_z \end{bmatrix}. \quad (5)$$

The intrinsic matrix of size $[3 \times 3]$ contains the pixel coordinates of the image center, also known as the principal point (u_o, v_o), the scaling factor k, which defines the number of pixels per unit distance in image coordinates, and the source-to-image distance SID, also known as the focal length, f of the C-arm (in meters). The extrinsic matrix of size $[3\times4]$ is identified by the transformation needed to align the world coordinate system to the camera coordinate system. This means that a translation vector, t, and a rotation matrix, R,

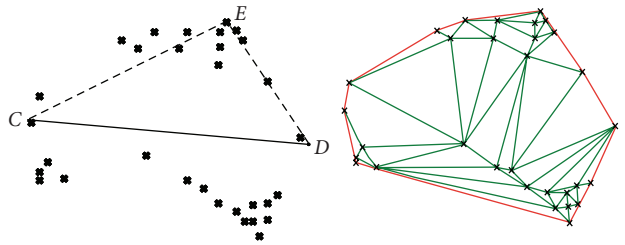

Figure 7: Convex Hull from a set of unorganized points.

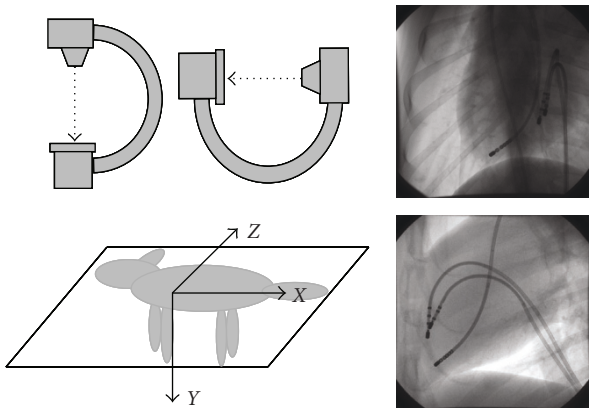

(a) (b)

Figure 8: (a) Typical monoplane C-arm fluoroscope and coordinate system centered at the tip of the reference catheter electrode. Biplane images are obtained by rotating the C-arm at two perpendicular positions. (b) Sample diastolic images for posterior and left lateral, respectively.

need to be found in order to align the corresponding axis of the two reference frames. Imaging parameters such as focal length, primary and secondary rotation angles image pixel spacing and size are obtained from the accompanied DICOM image files. This allows us to have a close enough estimate of the C-arm pose for a particular viewing angle.

Spatial reconstructions from biplane geometry evolved as important tools for morphological analyses of vessels or catheters in both cardiology and neurology domains [14–19]. From the known imaging geometry and using the point correspondences established by the epipolar constraint, any point visible in both projections can be spatially reconstructed by retracing the projection rays back to the point of their intersection. This can be achieved after successful calibration of the C-arm geometry. Since the reconstructed rays often miss this point due to slight reconstruction or calibration errors, usually their closest location is approximated. This is known as a stereo triangulation procedure (see Figure 6). Using the manual clicked tip electrode center coordinates, as well as the initial parameters of the C-arm gantry, we optimized the final 3D coordinates using the triangulation method. Details are omitted here for the sake of brevity.

2.4. Convex (Quick) Hull Algorithm. The tip-electrode coordinates in the monoplane images are collected and used

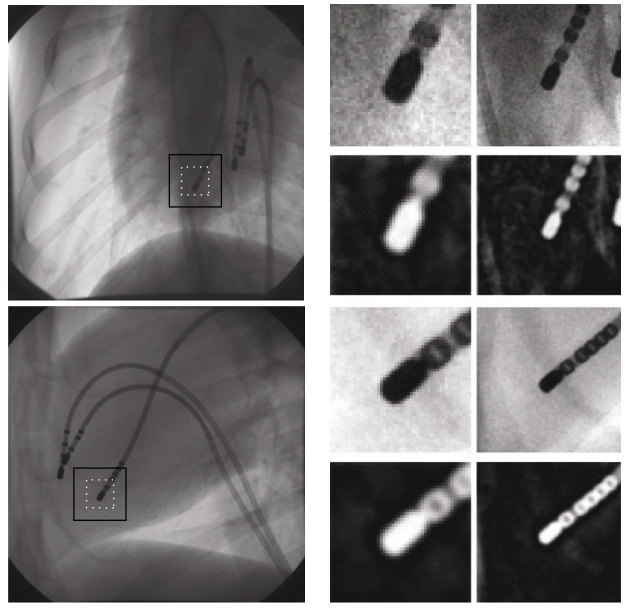

(a) (b)

Figure 9: (a) Template and search boxes defined around the centroid of the tip-electrode in the posterior and left lateral views respectively. (b) The final images from the 3-step filter applied to the template and search boxes respectively. Note the suppression of background in the images.

to form a 3D volume using a convex hull algorithm. The problem involves finding the smallest convex polygon containing all the points of S, given a set S of n points in multidimensional space [20]. The algorithm can be described briefly for 2D points as seen in Figure 7: Select the farthest points (left and right) from the data set (2D) and draw a line between them. We examine a set of points lying on the same side of the line (CD). In this set, select the point E that is located furthest away from the line CD. This point will also belong to the convex hull, since it cannot be included in a triangle. Moreover, we can remove all the points inside the triangle (CDE) and split the remaining points into two subsets: one with the points on the left of line (CE), and the other set containing points on the right of line (CE). The iterative process is repeated in these two subsets. Once the outer shell of the hull is established, we can analyze the set of data points located under the line segment (CD) in the same manner. Similar procedure can be expanded to the 3D scenario [14]. The convex hull will have an empty interior and is the method of choice in this paper. It is quick to implement and represents well the endocardial surface of cardiac chambers. Further, it was thought to be a good initial step for verifying the feasibility of our approach.

3. Experiments and Results

3.1. Mongrel Dog Experiment. We begin this section by recalling that our primary objective was to develop and test a mapping technique based on multiview measurements of electrode sites and on the reconstruction of the cardiac

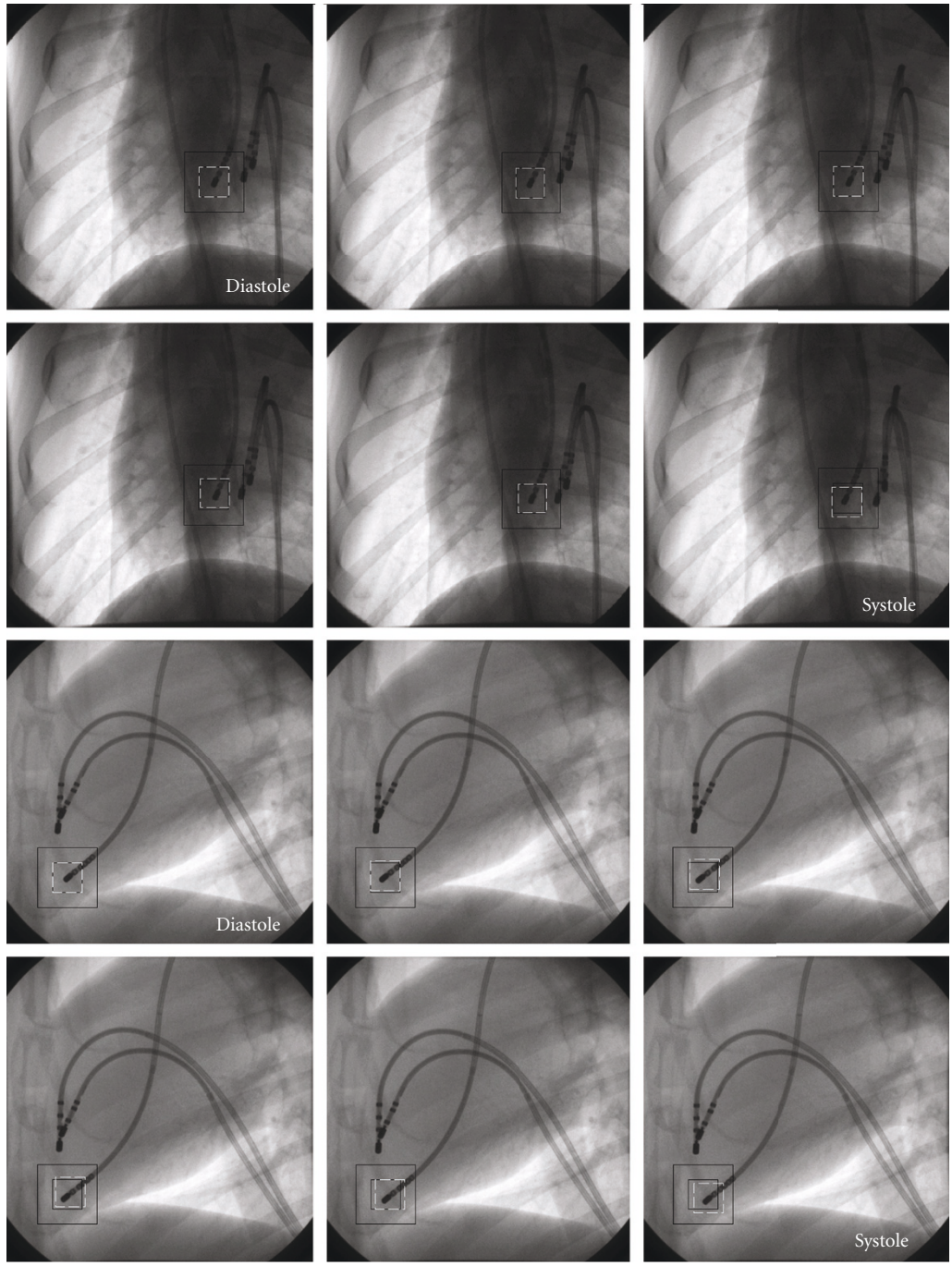

Figure 10: (*Top two rows*) Sample tracking results for the posterior view between diastole and systole. Random middle images are shown between the two cardiac phases. (*Bottom two rows*) Example images for the left lateral view.

chamber of interest. Here, the reconstruction uses a full perspective projection model coupled with surface fitting Convex Hull algorithm. Our overall methodology mimics the *CARTO XP* technology but only requires cost-effective standard catheters and a monoplane C-arm fluoroscope.

An animal experiment was carried out at Sacré Coeur Hospital, Montreal, Canada. Our experimental protocol met the institutional requirements of animal experimentation. A mongrel dog was anesthetized and laid on its right side on a fluoroscopy table (Integris Allura, Philips Inc.). A reference catheter and a pacing catheter were inserted into the right ventricle, close to the septal wall. The role of the reference catheter was to define an origin for our 3D coordinate system that is not affected by the displacement of the heart due to respiration or by the displacement of the animal or the X-ray system. The role of the pacing catheter was to produce a simple electrical activation sequence so as to validate the isochronal maps. Finally, a standard 7-French

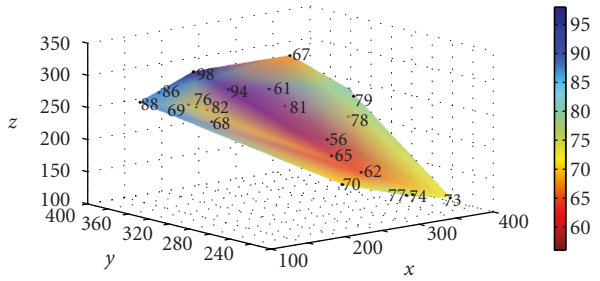

Figure 11: Three-dimensional convex hull of left ventricle obtained using the triangulation and perspective camera model. The (•) symbol represents the tip electrode coordinates of the mapping catheter which was moved to 20 different locations. Activation times were linearly interpolated and color coded with a red color signifying earliest activation time.

RF ablation catheter was inserted from the femoral vein into the left ventricle of the dog. During the course of the experiment, this mapping catheter was moved to 20 different sites (point-by-point) within the ventricle in order to obtain electrical and geometrical data from sufficient sites to map the activation sequence. Electrograms were recorded with the mapping catheter and the reference catheter using a multichannel analog-to-digital (A/D) converter card (PCI DAS-1001, Omega Engineering Inc.). The electrograms were saved in text file format. Specifications for the acquisition software were: 1000 samples/second, 1000 Hz bandpass, and 0.05 Hz high-pass and 450 Hz low-pass frequencies. Local activation time was measured as the difference in the times of the fastest negative deflections (dV/dt) seen in the two electrograms recorded with the reference catheter and the mapping catheter. The fluoroscopic image acquisition rate was set at 60 frames/second and images were recorded for about 2 seconds at the end of the expiration. The total fluoroscopy exposure time was thus 80 seconds which yielded a radiation dose of about 25 mGy to the mongrel dog. As illustrated in Figure 8, the monoplane fluoroscopic C-arm was rotated by 90° to acquire two images for each mapping site: a left lateral view (the C-arm in a vertical position) and a posterior view (the C-arm in a horizontal position). Images were recorded, in DICOM format, with a 512×512 pixel resolution. In the end, the data collected totaled twenty posterior view images, twenty left lateral view images, and the twenty electrograms. The MatLab (R2008a) software was used for all methods developed in this paper for prototyping purposes.

3.2. Temporal Tracking Results. The forty datasets were analyzed using our image extraction algorithm as outlined in Section 2.1. Thus, a total of forty diastole and systolic images were extracted from the DICOM datasets, plus additional images between the two cardiac phases. At this point, we manually clicked the tip electrodes of both the reference and mapping catheters in all diastole images and recorded them for the multiview 3D reconstruction method.

We simultaneously launched the automatic tracking algorithm once the mapping electrode was manually selected. The *template* and *search box* were instantiated followed by the application of the 3-step filter as seen in Figure 9. Registration was launched until the systolic image was reached. Estimated center results of the tip electrode were compared to an expert user click on the tip electrode for all images between diastole and systole. From Table 1, the total number of images analyzed for the posterior and left lateral datasets was 181 and 189, respectively. The average tip-electrode location error was 5.39 ± 6.75 pixels and 6.03 ± 7.67 pixels in the x and y directions for the posterior images. On the other hand, results improved for the left lateral view, as the average tip-electrode location error was 1.51 ± 1.53 pixels and 1.67 ± 1.65 pixels in the x and y directions, respectively. The excellent image quality for the left lateral images reflects the more precise tracking results.

In fact, three of the twenty posterior datasets contributed to the large maximum registration errors as seen in Table 1 as image quality and motion blur were ever present. A sample view of the tracking results is shown in Figure 10. The white dotted box shows the recovered positions after registration.

3.3. Multiview (Biplane) 3D Reconstruction Results. We subtracted the coordinates of the reference catheter for each mapping site so as to compensate for respiration and motion artifacts. The 3D coordinates of the tip-electrodes were optimized and recovered by the triangulation algorithm. We fitted the cloud of points using the 3D Convex Hull algorithm volume shown in Figure 11. After creating the 3D convex hull, the electrical activation times measured at each node were linearly interpolated over the surface of this volume and displayed as a color shift, using red for the earliest activation times and blue for the latest. The volume reflects the left ventricle of the mongrel dog.

So as to plot only the triangles that can be seen from a certain point of view, the normal to the surface of each triangle was calculated (the normal points outward), and if its dot product with the observation point vector was positive, the triangle was retained. For example, for the posterior view (XY plane), we retained all the nodes associated with a triangle whose normal component in the Z direction is positive. Similarly, for the left lateral (XZ) plane, we retained the nodes associated with a triangle whose normal component in the Y direction is negative. The fusion between the 2D isochronal activation map and the fluoroscopic image was performed in a 6-step process (see Figure 12), as outlined in the following.

(1) The nodes visible from the given point of view are identified using the Convex Hull data, and their 2D coordinates are retained (e.g., for the posterior view, the nodes are in the XY plane).

(2) The activation times of the visible nodes are positioned in a matrix, at the 2D coordinate locations of the nodes.

(3) The Delaunay method is used to organize the set of visible points as a set of triangles and cubic interpolation is applied to interpolate the activation times inside each triangle.

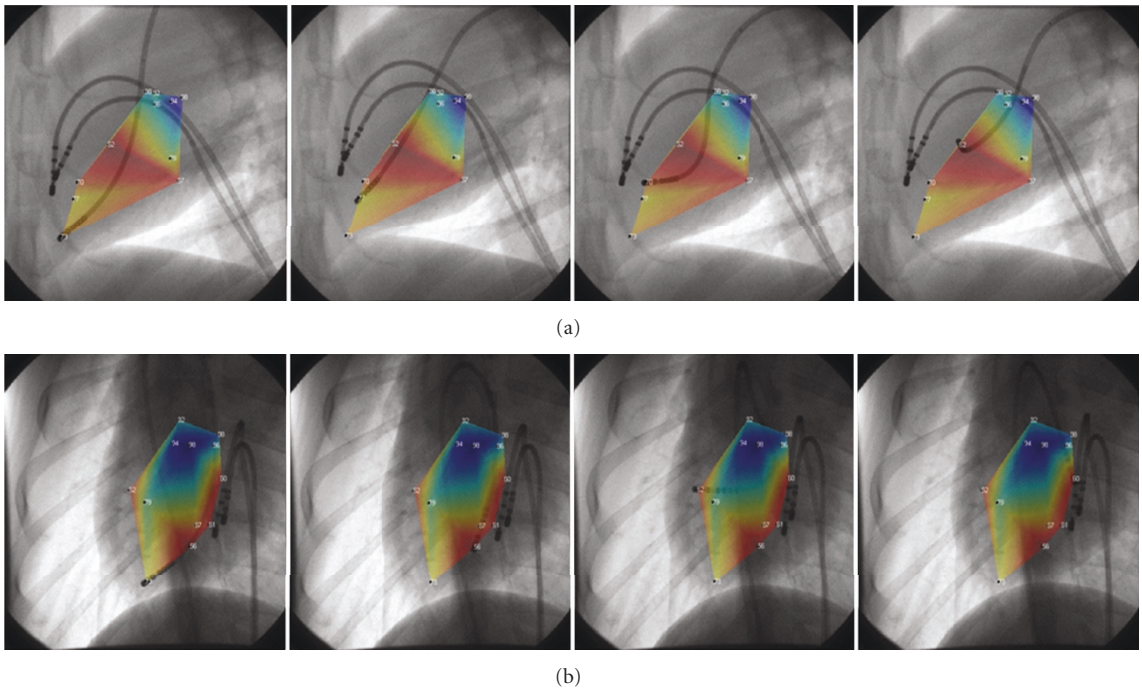

(a)

(b)

Figure 12: (a) Isochronal map superimposed on the diastolic images of the first four datasets for the left view and (b) posterior view.

Table 1: Temporal tracking results for both posterior and left lateral datasets.

Posterior View: tip-electrode detection			Left Lateral View: tip-electrode detection		
Number of images tracked:		181	Number of images tracked:		189
Registration errors (in pixels)			*Registration errors (in pixels)*		
	x	y		x	y
Min	0.04	0.01	Min	0.02	0.01
Max	41.9	41.8	Max	11.8	9.30
Mean	5.39	6.03	Mean	1.51	1.67
Std	6.75	7.67	Std	1.53	1.65

(4) In order to fuse the isochronal map to the $[512 \times 512]$ size fluoroscopic image, the borders of the above matrix are completed with zeros to achieve the same size as the image.

(5) The values of the $[512 \times 512]$ activation time matrix are scaled so that the maximum value is equal to 64 (which correspond to blue) and the minimum value is equal to 0 (which correspond to red).

(6) The scaled activation time matrix is used to create an RGB color matrix (using a red-to-blue color map), which is finally plotted over the fluoroscopic image with a 30% transparency ratio (30% for the color isochronal map and 70% for the grayscale fluoroscopic image).

From Figure 12, earliest activation times are clearly closest to the stimulation catheter (near the reference catheter). The posterior view also shows that the isochronal map followed the contour of the mapping catheter, which corresponds to the contour of the left ventricular cavity.

3.3.1. Present Method Advantages/Limitations versus the CARTO XP Technology. Since the *CARTO XP* nonfluoroscopic technology provides contact-based sequential acquisition of endocardial signals and reconstruction of 3D electroanatomical maps, this can be time consuming in terms of acquisition. However, this factor is operator dependent, and in experienced hands final geometry of a cardiac chamber can be obtained within 30 minutes [21]. More important, the instability of the catheter used for timing intracardiac activation and major patient movements relative to the location pad may render the entire map inaccurate for subsequent use, requiring the construction of a whole new map. For established indications, the major limitation for broader use of electroanatomical mapping in catheter ablation procedures at the present time is the associated cost.

This is further confounded by the high cost of the mapping catheter. In terms of typical ventricular tachycardia ablation procedures, authors in [22] indicate total average procedure time of 232 ± 56 minutes with fluoroscopy time of 10 ± 8 minutes.

The major drawback of our methodology is the use of fluoroscopy in order to reconstruct an anatomical 3D structure when compared to *CARTO XP*. Data acquisition took approximately 30–40 minutes, with about an additional 10–15 minutes of manual selection of the tip-electrodes, filtering, and temporal tracking for all image frames between diastole and systole. Also, the sequential measurements of the horizontal and vertical fluoroscopic images were not as accurate as simultaneous measurements with a true biplane fluoroscope as the vertical position of the reference catheter showed a difference of 4 ± 17 pixels in the twenty posterior and left lateral images. This relatively small difference can be explained by motion artifacts (respiration, heartbeat, subject displacement) and fluoroscope misalignment. However, we provide an added advantage by introducing 2D isochronal activation maps superimposed over the corresponding fluoroscopic images in the diastolic phase. These isochronal maps accurately depicted the progression of the electrical activation away from the pacing catheter. Furthermore, our entire methodology is cost efficient and this is important as the availability of expensive systems such as *CARTO XP* is still limited in developing countries [21].

4. Conclusion

We introduced a multiview method of a fluoroscopic navigation system to guide RF catheter ablation of cardiac arrhythmias. This initial prototype allowed us to: (1) localize in 3D the mapping catheter tip-electrode from two-view fluoroscopic images; (2) automatically extract important images of the cardiac phase, (3) measure the local activation times on the electrograms recorded with the catheter at multiple sites, and (4) superimpose over the fluoroscopic images, isochronal maps depicting the electrical activation sequence from which the cardiologist could precisely localize the arrhythmogenic site with respect to the RF catheter. As a plus, we present a single-click tracking algorithm that could estimate the locations of the tip-electrode in images following diastole. Our overall methodology strikes a balance between efficiency and robustness of a common multiview vision problem applied to medicine. Nevertheless, the true effectiveness of our method will be determined on patient data validation and experimentation.

Acknowledgment

The author would like to thank Dr. Pierre Savard, from École Polytechnique, Canada, for providing the image datasets and valuable suggestions.

References

[1] E. C. Stecker, C. Vickers, J. Waltz, et al., "Population-based analysis of sudden cardiac death with and without left ventricular systolic dysfunction: two-year findings from the Oregon sudden unexpected death study," *Journal of the American College of Cardiology*, vol. 47, no. 6, pp. 1161–1166, 2006.

[2] A. C. Lardo, H. Halperin, C. Yeung, P. Jumrussirikul, E. Atalar, and E. McVeigh, "Magnetic resonance guided radiofrequency ablation: creation and visualization of cardiac lesions," in *Proceedings 1st International Conference on Medical Image Computing and Computer-Assisted Interventation (MICCAI '98)*, pp. 189–196, Cambridge, Mass, USA, October 1998.

[3] A. C. Lardo, E. R. McVeigh, P. Jumrussirikul, et al., "Visualization and temporal/spatial characterization of cardiac radiofrequency ablation lesions using magnetic resonance imaging," *Circulation*, vol. 102, no. 6, pp. 698–705, 2000.

[4] E. Chu, A. P. Fitzpatrick, M. C. Chin, K. Sudhir, P. G. Yock, and M. D. Lesh, "Radiofrequency catheter ablation guided by intracardiac echocardiography," *Circulation*, vol. 89, no. 3, pp. 1301–1305, 1994.

[5] Y. Sun, S. Kadoury, Y. Li, et al., "Image guidance of intracardiac ultrasound with fusion of pre-operative images," in *Proceedings of the 10th International Conference on Medical Imaging and Computer-Assisted Intervention (MICCAI '07)*, vol. 4791 of *Lecture Notes in Computer Science*, pp. 60–67, Brisbane, Australia, October-November 2007.

[6] R. Razavi, D. L. G. Hill, S. F. Keevil, et al., "Cardiac catheterisation guided by MRI in children and adults with congenital heart disease," *The Lancet*, vol. 362, no. 9399, pp. 1877–1882, 2003.

[7] R. Kato, L. Lickfett, G. Meininger, et al., "Pulmonary vein anatomy in patients undergoing catheter ablation of atrial fibrillation: lessons learned by use of magnetic resonance imaging," *Circulation*, vol. 107, no. 15, pp. 2004–2010, 2003.

[8] J. M. Lacomis, W. Wigginton, C. Fuhrman, D. Schwartzman, D. R. Armfield, and K. M. Pealer, "Multi-detector row CT of the left atrium and pulmonary veins before radio-frequency catheter ablation for atrial fibrillation," *Radiographics*, vol. 23, pp. S35–S48, 2003.

[9] P. Fallavollita, P. Savard, and G. Sierra, "Fluoroscopic navigation to guide RF catheter ablation of cardiac arrhythmias," in *Proceedings of the 26th Annual International Conference of the IEEE Engineering in Medicine and Biology (EMBC '04)*, vol. 3, pp. 1929–1932, San Francisco, Calif, USA, September 2004.

[10] E. Franken, P. Rongen, M. Van Almsick, and B. Ter Haar Romeny, "Detection of electrophysiology catheters in noisy fluoroscopy images," in *Proceedings of the 9th International Conference on Medical Image Computing and Computer-Assisted Intervention (MICCAI '06)*, vol. 4191 of *Lecture Notes in Computer Science*, pp. 25–32, Copenhagen, Denmark, October 2006.

[11] V. I. Ponomarev and A. B. Pogrebniak, "Image enhancement by homomorphic filters," in *Applications of Digital Image Processing XVIII*, vol. 2564 of *Proceedings of SPIE*, pp. 153–159, San Diego, Calif, USA, July 1995.

[12] P. Perona and J. Malik, "Scale-space and edge detection using anisotropic diffusion," *IEEE Transactions on Pattern Analysis and Machine Intelligence*, vol. 12, no. 7, pp. 629–639, 1990.

[13] T. S. Yoo, M. J. Ackerman, W. E. Lorensen, et al., "Engineering and algorithm design for an image processing Api: a technical report on ITK—the Insight Toolkit," *Studies in Health Technology and Informatics*, vol. 85, pp. 586–592, 2002.

[14] Z. Zhang, "Determining the epipolar geometry and its uncertainty: a review," *International Journal of Computer Vision*, vol. 27, no. 2, pp. 161–195, 1998.

[15] P. H. S. Torr and D. W. Murray, "The development and comparison of robust methods for estimating the fundamental matrix," *International Journal of Computer Vision*, vol. 24, no. 3, pp. 271–300, 1997.

[16] G. Shechter, *Respiratory motion of the heart: implications for magnetic resonance coronary angiography*, Ph.D. dissertation, 2003.

[17] K. Sprague, M. Drangova, G. Lehmann, et al., "Coronary x-ray angiographic reconstruction and image orientation," *Medical Physics*, vol. 33, no. 3, pp. 707–718, 2006.

[18] N. Sang, W. Peng, H. Li, Z. Zhang, and T. Zhang, "3D reconstruction of the coronary tree from two X-ray angiographic views," in *Medical Imaging 2006: Image Processing*, vol. 6144 of *Proceedings of SPIE*, San Diego, Calif, USA, February 2006.

[19] C. Blondel, G. Malandain, R. Vaillant, and N. Ayache, "Reconstruction of coronary arteries from a single rotational X-ray projection sequence," *IEEE Transactions on Medical Imaging*, vol. 25, no. 5, pp. 653–663, 2006.

[20] C. B. Barber, D. P. Dobkin, and H. Huhdanpaa, "The quickhull algorithm for convex hulls," *ACM Transactions on Mathematical Software*, vol. 22, no. 4, pp. 469–483, 1996.

[21] F. Duru, "CARTO three-dimensional non-fluoroscopic electroanatomic mapping for catheter ablation of arrhythmias: a useful tool or an expensive toy for the electrophysiologist?" *Anadolu Kardiyoloji Dergisi*, vol. 2, no. 4, pp. 330–337, 2002.

[22] Y.-G. Li, Q.-S. Wang, G. Grönefeld, et al., "Refinement of CARTO-guided substrate modification in patients with ventricular tachycardia after myocardial infarction," *Chinese Medical Journal*, vol. 121, no. 2, pp. 122–127, 2008.